THE JOURNAL OF PHYSICAL CHEMISTRY B
A JOURNAL OF THE AMERICAN CHEMICAL SOCIETY

pubs.acs.org/JPCB

Article

# From Molecule to Aggregate: Understanding AIE through Multiscale Experimental and Computational Techniques

Deeksha Rajput,[†] Sanyam,[†] Gaurav Rawat, Priyanshu Sorout, Sriram Kanvah,* and Anirban Mondal*

Cite This: https://doi.org/10.1021/acs.jpcb.4c03744

Read Online

ACCESS | Metrics & More | Article Recommendations | Supporting Information



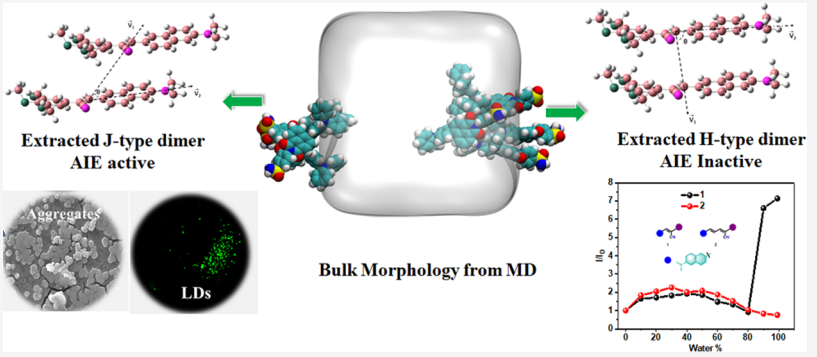


**ABSTRACT:** Aggregation-induced emission (AIE) phenomena have garnered significant attention due to their applications in various fields, ranging from materials science to biomedicine. Despite substantial progress, the underlying mechanism governing the AIE activity of molecules remains elusive. This study employs a comprehensive and multiscale approach, combining experimental and theoretical methodologies, to discern the determinants of AIE activity. Our investigations involve synthesizing four organic molecules with D-$\pi$−A-D architecture, accompanied by quantum mechanics (QM) and molecular dynamics (MD) simulations, providing a deep understanding of the interactions within aggregates. The symmetry-adapted perturbation theory (SAPT) calculations further corroborate our findings, revealing a clear correlation between AIE activity and the type of aggregate formed. Specifically, we demonstrate that AIE-active molecules exhibit a distinctive J-type aggregation characterized by enhanced emission from the $S_1$ state. In contrast, AIE-inactive molecules adopt an H-type aggregate configuration, where the emission from the $S_1$ state is constrained. In addition, we investigated the subcellular localization of the molecules, revealing localization within the lipid droplets. Our findings contribute to the fundamental understanding of AIE phenomena and provide insights into the design principles for AIE-active materials with potential applications in advanced sensing and imaging technologies.

## INTRODUCTION

Aggregation Induced Emission (AIE) describes a counter-intuitive phenomenon observed in certain organic luminophores wherein the emission intensity enhances upon the formation of nanoparticles or aggregate compared to the solution state.[1−4] The mechanism of aggregation-induced emission (AIE) is primarily based on the interplay between radiative and nonradiative decay pathways. In isolated states or dilute solutions, molecules often exhibit fast nonradiative decay due to efficient conical intersection (CI) crossing, wherein electronic energy is rapidly dissipated as vibrational energy within hundreds of femtoseconds. In contrast, in aggregated states or solid phases, the nonradiative decay is suppressed because molecules encounter barriers to reaching the CI, which are more difficult to overcome than liquid states. This reduction in nonradiative decay allows radiative decay, dependent on the transition dipole moment, to dominate. Notably, the transition dipole moment can be significantly diminished in H-aggregates, resulting in a slower radiative decay. Consequently, the AIE effect arises as the aggregated state favors radiative decay over the suppressed nonradiative channels, leading to enhanced emission intensity compared to the solution phase.[5] This phenomenon contrasts most fluorophores' prevalent aggregation-caused quenching (ACQ) properties. The enhanced emission arises from restricted intramolecular motions (RIM) within the aggregated molecules. These molecules can twist and rotate freely in solution, facilitating nonradiative decay pathways. However, when they pack closely in the aggregated state, these motions become restricted, hindering the nonradiative pathways and allowing more efficient conversion of the absorbed energy into light

Received: June 5, 2024
Revised: November 5, 2024
Accepted: November 25, 2024

emission.[6] The mechanism of AIE is multifaceted and involves several contributing factors. While ref 6 highlights the concept of restricted intramolecular rotation leading to enhanced emission in the aggregated state, this explanation is not entirely sufficient for the context of our study. Specifically, the orientation and packing of molecules within the aggregates significantly influence the emission properties. As detailed in the reference,[5] AIE can also arise from factors such as restriction of intramolecular vibration, twisted intramolecular charge transfer, and specific molecular interactions within the aggregate. Reference[7] further elaborates on the role of molecular orientation and environmental effects on AIE. Several factors promote aggregation-induced emission: the molecular structure, twisted conformations, and bulky substituents promoting AIE. Notably, the nature of $\pi-\pi$ stacking interactions can yield potent AIE enhancement.[4,8−11] Also, it is worth mentioning that $\pi-\pi$ stacking may also serve to facilitate nonradiative dissipation pathways. These interactions occur between aromatic rings, enhancing electronic and vibrational coupling, promoting nonradiative relaxation. The proximity of aromatic rings in $\pi-\pi$ stacked configurations allows for efficient energy transfer and quenching of excited states, enabling electrons to return to the ground without emitting radiation.

Considering the unique emission in aqueous media, the AIE behavior has attracted attention to investigations of various cellular processes, theragnostic applications, or analyte detection with high sensitivity and selectivity.[12,13] In addition, AIE luminophores offer improved brightness and efficiency in OLEDs, enhancing display performance, among others.[14−17] Understanding the molecular mechanism behind aggregation-induced emission is paramount in designing new molecules with enhanced optical properties. $\alpha$-cyanodiarylethenes, distinguished by the presence of a nitrile group on the double bond, exemplify this importance due to their pronounced AIE behavior.[14] Unraveling the intricate mechanisms driving AIE not only elucidates the fundamental principles governing light emission in aggregated states but also paves the way for the strategic development of novel molecular architectures. By comprehending how specific molecular structures influence the aggregation-induced emission process, researchers can engineer tailored designs to optimize AIE properties. Moreover, such insights foster the exploration of innovative design strategies, enabling the synthesis of molecules with superior performance and versatility for various applications. As AIE continues to garner attention for its promising applications in fields ranging from optoelectronics to biomedicine, a deep understanding of its molecular underpinnings is indispensable for propelling the advancement of functional materials and technologies.

Despite numerous studies and efforts, the molecular mechanisms governing aggregation-induced emission remain elusive, leaving a critical gap in our understanding of this phenomenon. While research endeavors have delved into molecular simulations[18,19] to probe the AIE behavior, definitive conclusions have yet to be drawn. The primary difficulty is distinguishing whether a particular molecule will exhibit AIE, which remains unanswered. For instance, while some works have elucidated the factors that render molecules AIE inactive,[20] others have highlighted the role of acceptors or the formation of specific aggregates.[7,21] Ref 5 comprehensively outlines the theoretical framework and critical factors contributing to AIE, such as the restriction of intramolecular motion and changes in electronic states upon aggregation. Additionally, the effect of specific molecular features, including acceptor groups,[21,22] molecular orientation,[7] and hydrogen bonding[23,24] on the intensity and efficiency of AIE emission have been explored. These studies collectively provide a detailed understanding of the multifaceted nature of AIE, emphasizing both the intrinsic molecular properties and the external environmental factors that affect emission behavior. Nevertheless, these findings do not offer a unified explanation for the occurrence of AIE across diverse molecular structures. Molecular simulations and theoretical studies have contributed valuable insights into the aggregation process and its correlation with emission intensity. However, the intricate interplay of molecular interactions, conformational dynamics, and energy transfer mechanisms in the aggregated state remains a complex puzzle. Thus, the quest for deciphering the molecular basis of AIE persists, necessitating interdisciplinary efforts to unravel its mysteries and guide the rational design of AIE-active molecules for future applications.

Our research combines experimental and computational methods to understand the AIE and ACQ observations. We utilize a series of arylethylene scaffolds, **1**−**4**, characterized by D-$\pi$−A-D architecture. This approach allows us to comprehensively understand the factors influencing AIE and ACQ in these molecules. We have used computational tools such as quantum mechanical (QM) calculations and molecular dynamics (MD) simulations to conduct theoretical analyses, including calculations of oscillator strength, charge transfer numbers, and slip angle assessments in an explicit solvent medium. These calculations show the transition dynamics between singlet states directly influencing the emission behavior. Notably, our slip angle calculations elucidate the significance of molecular orientation and alignment in solution, offering insights into the AIE activity of specific molecules. Additionally, complementary Symmetry-Adapted Perturbation Theory (SAPT) calculations further validate our findings, reinforcing the robustness of our approach in elucidating the AIE mechanism. We also explored the potential of synthesized $\pi$-conjugated molecules for probing subcellular compartments. Long Stokes shifts, easy structural tunability, favorable photophysical properties, and biocompatibility contribute valuable information to understanding the subcellular milieu and facilitates visualization of cellular compartments.[25−28] Through this multidisciplinary investigation, we aim to advance the fundamental understanding of AIE and ACQ phenomena and facilitate the rational design of functional materials with tailored optical properties.

## EXPERIMENTAL SECTION

**Materials and Methods.** The consumables and chemicals required for synthesizing the molecules were purchased from local suppliers, namely Aldrich, BLD Pharm, TCI Chemicals, FinarChem, and SD Fine-Chem. The synthesized fluorophores were characterized using $^{1}$H and $^{13}$C NMR (Bruker Avance 500 MHz) in chloroform-D with TMS as an internal standard. High-resolution mass spectrometry (HRMS) data were recorded using a Water Synapt G2S ESI Q-ToF mass spectrometer. Absorption studies were performed on a Shimadzu UV−vis 3600i instrument, and steady-state fluorescence studies were measured using a Horiba Jobin Yvon Fluorolog-3 spectrofluorometer. Lifetime measurements were performed on a Horiba Delta-Flex time-correlated single-photon counting (TCSPC) spectrometer. The sample


https://doi.org/10.1021/acs.jpcb.4c03744
J. Phys. Chem. B XXXX, XXX, XXX−XXX

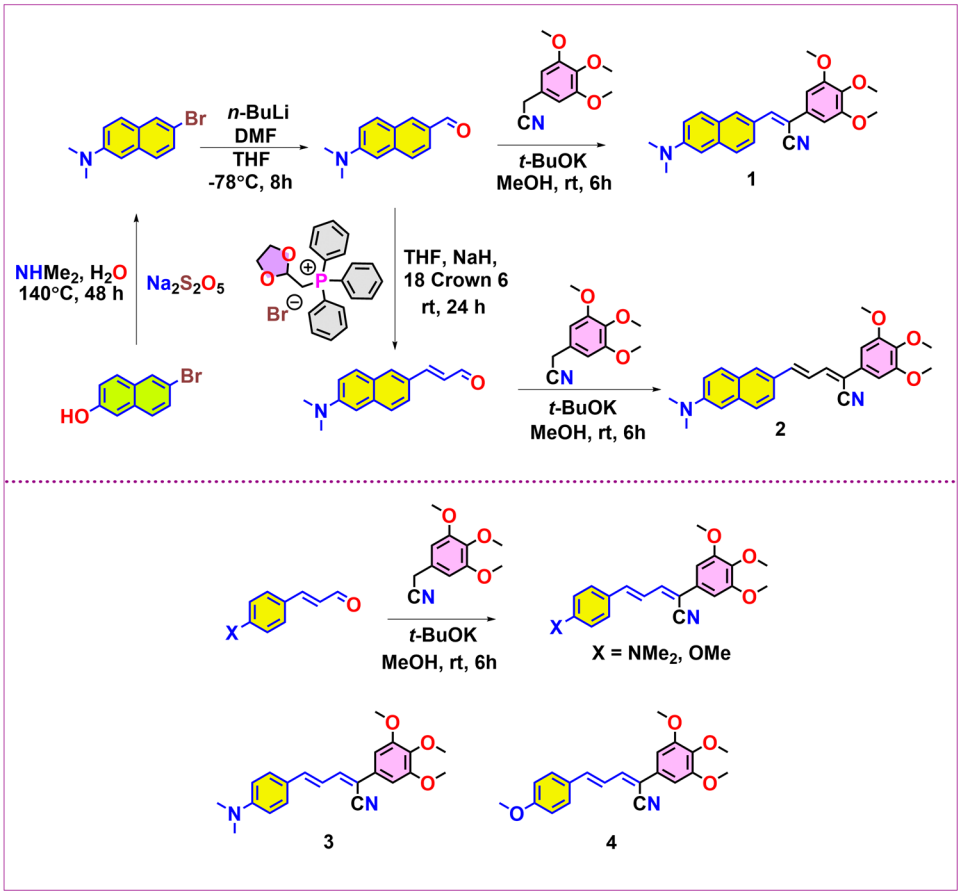


**Figure 1.** Synthetic scheme for the preparation of $\alpha$-cyanodiarylethenes. The spectral characterization details are given in the Supporting Information.

concentrations used for the fluorescence studies were in the order of 10 $\mu$M. The excitation wavelength for recording the emission spectra was typically kept at the absorption maxima of the samples under investigation. DLS measurements were performed using a Malvern Zetasizer Ultra instrument. The DLS samples were prepared in water and filtered through a microfilter; air bubbles were removed before measurements. SEM measurements were performed using an advanced analytical FE-SEM instrument (JEOL JSM-7900F).

**Cell Culture and Co-Localization.** COS-7 cells were cultured in DMEM (Dulbecco's Modified Eagle Medium; Gibco) supplemented with 10% FBS (Fetal Bovine Serum; Gibco) at 37 °C in a humidified environment with 5% $CO_2$. A total of 0.5 × $10^5$ cells were seeded on a 35 mm glass-bottom dish, and the following day, the cells were treated with the synthesized fluorophores 5 min before commencing live-cell imaging. For the colocalization experiment, after treatment with the fluorophores (1 $\mu$M), the cells were incubated with commercially available Nile red. The lasers used for excitation were 405 nm for **1**−**4** and 561 nm for Nile red. Emission signals were collected using both a HyD and PMT detector.

**Cell Viability Assay.** The cytotoxicity of the probes was confirmed using the MTT (3-(4,5-dimethylthiazol-2-yl)-2,5-diphenyltetrazolium bromide) assay in COS-7 cells. COS-7 cells were seeded in a 96-well plate with DMEM supplemented with 10% FBS and incubated in a 5% $CO_2$ incubator at 37 °C for 24 h. The cells were then treated with the fluorophores, **1**−**4**, at different concentrations of 0.25, 0.5, 1.0, 2.0, and 4.0 $\mu$M. Cells without any fluorophore served as a negative control. As the stock solutions of the probes were prepared in DMSO and added to cell media (DMEM and 10% FBS), a DMSO control was also included with the same percentage of DMSO (0.5% v/v). After a 24h incubation with the probes, the medium was removed entirely, and the cells were incubated in 100 $\mu$L of MTT solution (0.5 mg/mL) for 4h, leading to the formation of formazan crystals due to the reduction of MTT by viable cells. The MTT solution (75 $\mu$L) was gently removed with a pipet without disturbing the purple-colored formazan crystals and redissolved in 75 $\mu$L DMSO. The absorbance was recorded at 570 nm using a PerkinElmer multimode plate reader. The triplet of each probe concentration was evaluated for the MTT assay. The percentage cell viability of the compounds was calculated with respect to the negative control (cells in DMEM and 10% FBS media)

**Data Analysis.** The live-cell images were analyzed and quantified using ImageJ software (nih.gov). The Pearson correlation coefficient (PCC) was calculated using the ImageJ coloc plugin for the colocalization experiment. Photophysical studies and cell viability assay data were plotted using Origin 9.1 software.

**Quantum Mechanical (QM) Calculations.** We conducted a comprehensive computational investigation on four experimentally synthesized organic molecules, the chemical structures shown in Figure 1. Ground state optimizations and frequency analysis for these complexes were performed at B3LYP/6-311+G(d,p) level of theory as implemented in the Gaussian09 program.[29] The earlier computational reports on similar molecules drove the choice of B3LYP functional.[30] The


https://doi.org/10.1021/acs.jpcb.4c03744
J. Phys. Chem. B XXXX, XXX, XXX−XXX

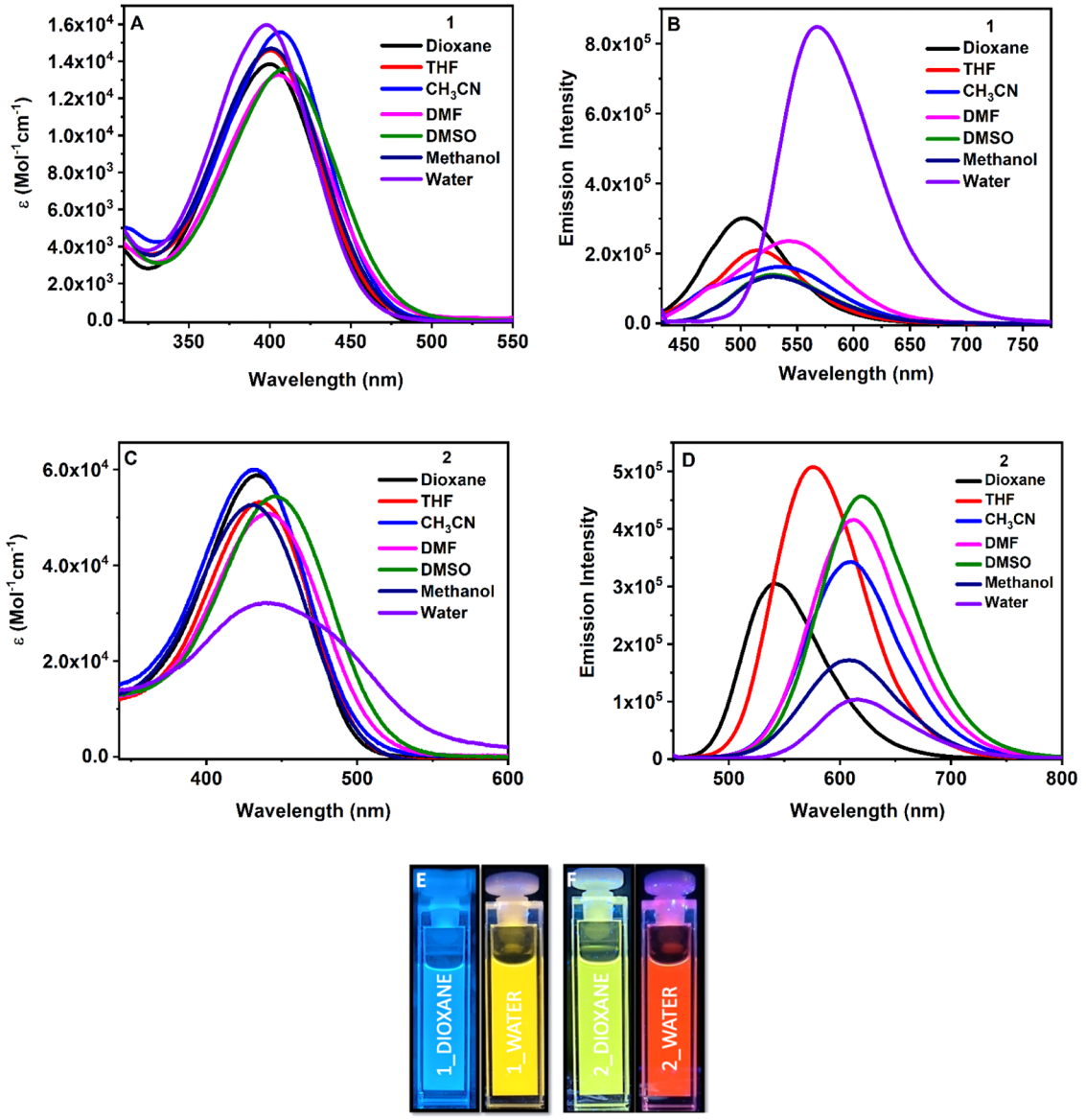


**Figure 2.** (A) Absorption and (B) emission spectra of **1** in different solvents; (C) Absorption and (D) emission spectra of **2** in different solvents. The solution colors (E) **1** and (F) **2** in dioxane and water were visualized under a UV lamp.

adiabatic geometry for the excited $S_1$ states was obtained using the B3LYP/6-31+G(d,p) method. The excited state optimization was carried out in three different solvents: water ($\varepsilon$ = 78.5), methanol ($\varepsilon$ = 32.6), and tetrahydrofuran (THF, $\varepsilon$ = 7.2) utilizing the Conductor-like Polarizable Continuum Model (CPCM).[31] We used the linear-response approach for the excited state structure optimization. To delve deeper into the excited state characters of these molecules, we performed charge transfer (CT) number analysis. As demonstrated in an earlier report,[21] the charge transfer nature of the molecule is inversely related to the AIE behavior. These calculations were performed utilizing the ORCA 5.0 program[32] utilizing the same combination of functional and basis set mentioned above. We additionally assessed the charge transfer properties by calculating the charge transfer number for the dimer. We optimized the dimer structure with dispersion corrections with the B3LYP/6-31+G(d,p) method using the Gaussian 09 software package. Subsequently, charge transfer calculations were performed using ORCA 5.0, which utilized the same functional and basis set. The optimized geometries of the investigated compounds are provided in the zipped folder of the Supporting Information.

**Molecular Dynamics Simulations.** These simulations utilized the all-atom-optimized potentials for liquid simulation (OPLS-AA) parameters. Lennard−Jones (LJ) parameters were used from the OPLS-AA force field,[33,34] complemented by a fudge factor of 0.5 for 1−4 interactions. We also used the atomic charges directly from the OPLS force field to maintain a consistent simulation setup. GROMACS simulation package generated the realistic molecular morphologies through MD simulations.[35,36] These simulations were carried out in three solvent conditions: water, tetrahydrofuran (THF), and methanol. System construction involved keeping a molecule at the center of the simulation box, surrounded by 1000 solvent molecules, subsequently followed by replication of the box in a 2 × 2 × 2 fashion in space. A comprehensive system comprising eight thousand solvent molecules with eight organic molecules was thus built. The initial configurations


https://doi.org/10.1021/acs.jpcb.4c03744
J. Phys. Chem. B XXXX, XXX, XXX−XXX

Table 1. Absorption and Emission Properties of the Synthesized Fluorophores (10 μM)[a]

| | | dioxane | THF | $CH_3CN$ | DMSO | DMF | $CH_3OH$ | water |
|---|---|---|---|---|---|---|---|---|
| 1 | $\lambda_{abs}$ (nm) | 399 | 400 | 406 | 405 | 409 | 401 | 398 |
| | $\lambda_{em}$ (nm) | 500 | 515 | 538 | 530 | 544 | 530 | 565 |
| | $\varepsilon$ | 13 850 | 14 551 | 15 567 | 13 564 | 13 283 | 14 633 | 15 959 |
| | $\Delta\upsilon$ ($cm^{-1}$) | 5062 | 5582 | 6043 | 5823 | 6067 | 6069 | 7426 |
| | $\phi$f | 0.013 | 0.014 | 0.009 | 0.011 | 0.016 | 0.007 | 0.02 |
| 2 | $\lambda_{abs}$ (nm) | 435 | 436 | 431 | 440 | 446 | 431 | 440 |
| | $\lambda_{em}$ (nm) | 541 | 575 | 608 | 613 | 619 | 608 | 615 |
| | $\varepsilon$ | 58 668 | 53 171 | 60 146 | 54 409 | 50 615 | 52 399 | 32 021 |
| | $\Delta\upsilon$ ($cm^{-1}$) | 4504 | 5544 | 6754 | 6414 | 6266 | 6754 | 6467 |
| | $\phi$f | 0.1 | 0.08 | 0.05 | 0.12 | 0.15 | 0.02 | 0.04 |
| 3 | $\lambda_{abs}$ (nm) | 427 | 427 | 425 | 439 | 435 | 427 | 427 |
| | $\lambda_{em}$ (nm) | 525 | 535 | 561 | 570 | 563 | 552 | 581 |
| | $\varepsilon$ | 17 860 | 21 775 | 18 472 | 13 550 | 18 181 | 16 775 | 10 084 |
| | $\phi$f | 0.03 | 0.03 | 0.03 | 0.04 | 0.03 | 0.02 | 0.04 |
| | $\Delta\upsilon$($cm^{-1}$) | 4371 | 4727 | 5704 | 5235 | 5226 | 5303 | 6207 |
| 4 | $\lambda_{abs}$ (nm) | 379 | 378 | 374 | 384 | 381 | 375 | 376 |
| | $\lambda_{em}$ (nm) | 433 | 462 | 463 | 442 | 463 | 450 | 500 |
| | $\varepsilon$ | 13 153 | 12 771 | 14 609 | 8969 | 9657 | 11 828 | 7921 |
| | $\Delta\upsilon$ ($cm^{-1}$) | 3290 | 4810 | 5139 | 3417 | 4648 | 4444 | 6595 |
| | $\phi$f | 0.007 | 0.001 | 0.0006 | 0.002 | 0.001 | 0.0007 | 0.001 |

[a]Units: $\varepsilon$ (molar extinction coefficient) = $Mol^{-1}$ $cm^{-1}$; Fluorescence quantum yields ($\phi_f$) were determined using reference standard Quinine hemisulfate ($\phi$ = 0.546 in water) for of **1** and **4**, using Rhodamine 6G ($\phi_f$ = 0.95 in ethanol) for **2** and Fluorescein ($\phi$f = 0.95 in water); $\Delta\upsilon$ is the measured Stokes shift in $cm^{-1}$.

underwent energy minimization employing the steepest-descent method. This preparatory phase was succeeded by an equilibration run extending over 5 ns in the NPT ensemble, complemented by a production run spanning 15 ns in the NVT ensemble. Both runs were executed at a controlled temperature of 300 K and a pressure of 1 bar. The simulations adhered to the NPT and NVT ensembles, incorporating a canonical velocity rescaling thermostat,[36] a Berendsen barostat[37] for pressure coupling, and the smooth particle mesh Ewald (PME) technique to address long-range electrostatic interactions. A time step of 0.001 ps facilitated the numerical integration of equations of motion, with nonbonded interactions computed using a real-space cutoff of 1 nm. The simulation outcomes involving methanol and tetrahydrofuran (THF) indicate that organic molecules are soluble in these solvents, as evidenced by the absence of molecular aggregation. THF and methanol were chosen as solvents due to their non-aggregating nature. In contrast, the molecules exhibited aggregation in water. To elucidate this phenomenon and to further characterize the type of aggregates formed, slip angle calculations, as discussed in ref 7 were conducted. Additionally, symmetry-adapted perturbation theory (SAPT) calculations were employed using psi4 program to further support theoretical evidence.[38]

## RESULTS AND DISCUSSION

Arylethylene derivatives (**1**−**4**) were synthesized and studied for their photophysical investigations. Compound **1** is a styryl derivative, and **2**, **3**, and **4** are the butadiene derivatives. All the molecules are characterized by a trimethoxyphenyl unit serving as an electron donor and moiety and an $\alpha$-cyano group serving as an acceptor. Additionally, **1**−**3** also have a dimethylamino donor group, **4** has a methoxy group. Such donor−acceptor scaffold is expected to contribute to the characteristic intramolecular charge transfer (ICT) behavior. The desired compounds were synthesized through Knoevenagel condensation using 3,4,5-trimethoxyphenyl acetonitrile with the corresponding aldehydes. The naphthalene-substituted carbaldehyde and cinnamaldehyde were synthesized using established procedures[39,40] (Figure 1). The detailed synthetic procedures with spectral characterization are provided in the Supporting Information.

**Absorption and Emission Properties.** We first evaluated the absorption and emission properties of naphthalene substituted $\alpha$-cyanodiaryl derivatives, as shown in Figure 2. Compound **1** absorbs at 399 nm in dioxane while its $\pi$-extended counterpart **2** absorbs at 435 nm, revealing the influence of the extended delocalization (Table 1). Compounds **3**−**4** absorb lower than 435 nm, and the lower absorption is attributed to decreased delocalization, with **4** being the lowest and **2** the highest. Further, the molecules are insensitive to the polarity variations in the surrounding environment. On the other hand, the molecules show solvatochromic emission properties with polarity variations and moderate bathochromic emission shifts. Compound **4** with the methoxy donor group exhibits the lowest emission wavelength, Stokes shift among the compounds, and compound **2** emits at the longest wavelength. The difference is attributed to extended delocalization (naphthalene vs phenyl), and a stronger electron-donating group (dimethylamino vs alkoxy) results in a greater extent of charge transfer (Figures 2 and S1−S2).

Emission is red-shifted in water for **1** with enhanced emission, but emission quenching is noted for compounds **2**-**4**. We also examined the fluorescence in the solid state (Figure S3 and Table S1), and compound **1** emits at 596 nm a bathochromic shift of 31 nm in the solid state compared to its emission in water. Compounds **2**−**4** show variable emission maxima with **2** (561 nm) and **3** at (540 nm) have hypsochromic emission to their respective solution states, while **4** emits at 529 nm more than what is observed in water (Figure S3). The quantum yield of fluorescence in solid state is


https://doi.org/10.1021/acs.jpcb.4c03744
J. Phys. Chem. B XXXX, XXX, XXX−XXX

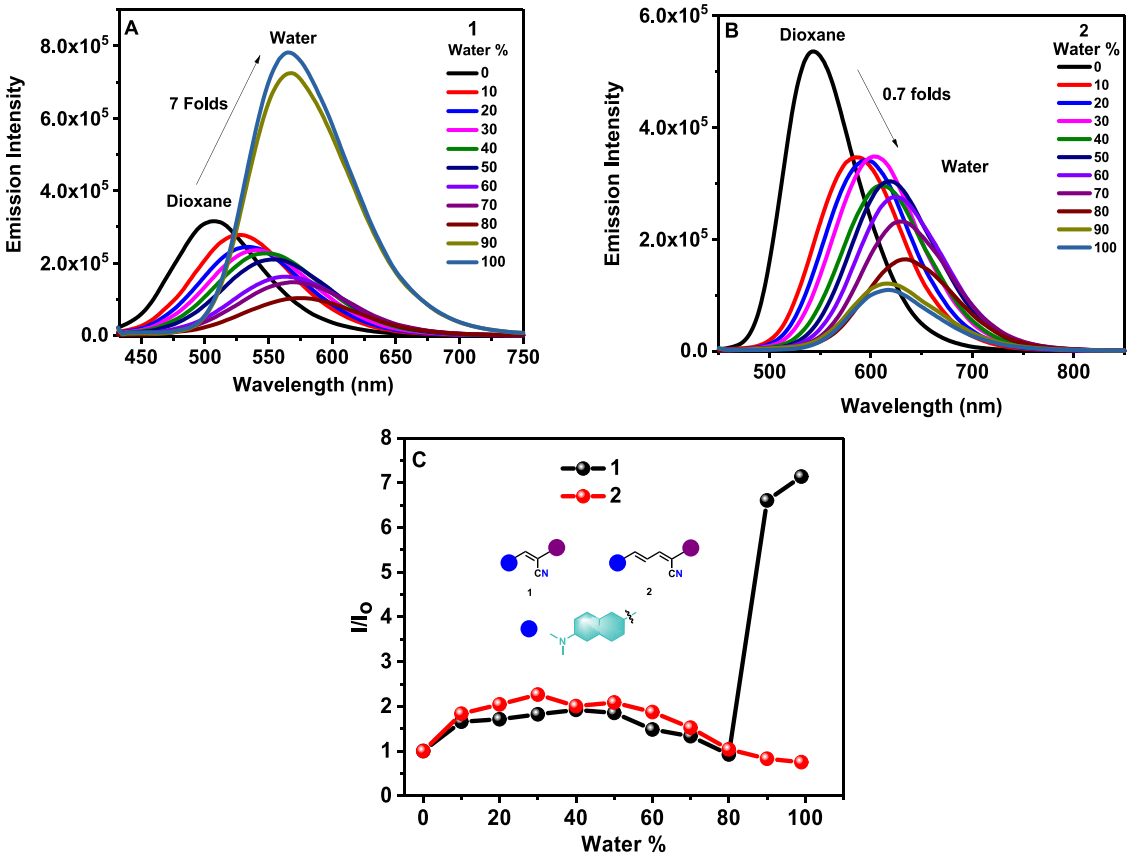


**Figure 3.** (A) Emission spectra of **1** in dioxane/water binary mixture; (B) Emission spectra of **2** in dioxane/water binary mixture; (C) I/Io vs water % plot to compare the AIE effect between **1** and **2**.

greater for compound **1** than the others and is attributed to the nature of the intermolecular packing and restricted torsional motions.

This behavior in water for the styryl derivative **1** is attributed to the characteristic aggregation-induced emission [6, 11]. To examine its aggregation effects, we studied its emission in dioxane (good solvent)-water (poor solvent) binary mixtures. Upon gradually adding water in dioxane (Figure 3), the molecule shows emission shifts from 500 to 565 nm attributed to the polarity changes followed by significant emission intensity enhancement over 7-folds when the percent water increases to 90%. Contrary to this, the $\pi$-extended **2** shows emission quenching with increased solvent polarity (Figure 3C). Both **1** and **2** have naphthalene moiety, which could also contribute to increased hydrophobicity. To assess if other dienes with simpler phenyl groups exhibit the AIE/ACQ, we tested with two other dienes **3** and **4**, containing *p*-dimethylaminophenyl and *p*-methoxyphenyl groups. Both the dienes show ACQ effects (Figure S2). All the molecules are hydrophobic and tend to form aggregates in aqueous media, but the emission intensity enhancement is only indicated for the cyanostilbene **1**. This ACQ effect is attributed to additional bonds contributing to the added flexibility. In **1**, such conformational flexibility is minimal, and the aggregation results in restricted molecular rotations. The average lifetime of **1** also shows an increase from 0.05 to 1.09 ns from dioxane to water attributed to the aggregate formation. The particle size of the formed aggregate was examined using dynamic light scattering (DLS), and the average size (Figure S4) ranged between 141 and 217 nm. The SEM images (Figure S5) also reveal the formation of aggregates along with changes in the morphology. Cyanostilbene, **1**, which shows the AIE character, reveals brick-like aggregates, whereas **2**, having extended vinyl conjugation, shows spherical aggregates. Molecule **3** shows oval to irregular aggregate formation, and **4** shows irregular shape. Aggregates are also formed with other molecules, as reflected by the rise in the average lifetime for **2**−**4**, but only **1** shows the AIE effect while **2**−**4** shows the ACQ. The lifetime spectral details of the derivatives are shown in Figure S6 and Table S2

**Quantum Mechanical Analysis.** Quantum mechanical analysis was conducted to shed light on the factors influencing the aggregation-induced emission activity of the studied molecules. Table 2 presents computed data, including wavelength, oscillator strength ($f$), and charge transfer (CT) numbers. A crucial aspect considered in this analysis was the oscillator strength, indicative of the likelihood of transition from the first singlet excited state ($S_1$). Molecules deemed AIE inactive often exhibit low oscillator strengths during emission,

**Table 2. QM Computed Properties of the Investigated Compounds**[a]

| compounds | wavelength (nm) | oscillator strength | $CT_{monomer}$ | $CT_{dimer}$ |
|---|---|---|---|---|
| 1 | 570.0 | 1.61 | 0.623 | 0.930 |
| 2 | 599.6 | 1.88 | 0.751 | 0.499 |
| 3 | 585.5 | 1.60 | 0.471 | 0.617 |
| 4 | 630.1 | 2.13 | 0.626 | 0.917 |

[a]The numbers are calculated using water as the solvent utilizing the CPCM solvent model.


https://doi.org/10.1021/acs.jpcb.4c03744
J. Phys. Chem. B XXXX, XXX, XXX−XXX

potentially hindering emission in the aggregated state. However, experimental and theoretical observations confirm that all the molecules emit within the visible region, with emission wavelengths in water solvent ranging from 500 nm (green) for compound **4** to 615 nm (red) for compound **2** (Table 1). The theoretical wavelength values closely match experimental measurements, providing strong evidence against emission outside the visible region as a cause for AIE inactivity. The other reason for AIE inactivity could be that the oscillator strength value might be too low even if the molecule emits in the visible region. Hence, the emission intensity from the $S_1$ state is very low. However, as we have observed experimentally, the emission intensity was high. Also, theoretically, we can support this finding due to the high oscillator strength values observed for all four compounds, ranging from 1.60 (lowest) for compound **3** to 2.13 (highest) for compound **4**. Furthermore, CT numbers were calculated to discern the nature of singlet states, distinguishing between charge transfer and locally excited states. While high CT numbers may suggest a molecule's AIE inactivity, it is not a definitive criterion. For instance, compound **1**, identified as AIE active, exhibited lower CT numbers than compound **3** in monomer configurations. But in the dimeric form, it possesses the highest CT number. Notably, these QM calculations were performed considering implicit solvent models, recognizing the influence of solvent environment and molecular orientation on AIE activity. Thus, our comprehensive QM analysis provides valuable insights into the AIE mechanism, highlighting the multifaceted interplay of molecular properties and environmental factors in dictating AIE behavior. Thus, we can conclude that the reasons for AIE inactivity do not include the low oscillator strength values, wavelengths outside the visible region, and high charge transfer numbers as observed in quantum mechanics.

To investigate the aggregation phenomenon, we utilized molecular dynamics (MD) simulations to generate morphologies. We plotted the radial distribution function (RDF) of the organic molecules' center of mass in water, THF, and methanol. From the RDF plot in Figure 4, the probability of molecules being in close proximity to one another in water, indicated by the height of the first peak, can be determined. Similarly, Figures S7 and S8 provide this probability in THF and methanol, respectively. Comparing the distances at which the first peak occurs in water (Figure 4), THF (Figure S7), and methanol (Figure S8), it is evident that organic molecules are in closer proximity, and the height of the first peak is higher in water. This indicates a higher probability of molecular aggregation in water than THF and methanol. Also, Figure S9 shows the initial and final configuration during the simulations in water for compound **1**. We have included detailed depictions of the dimer structures, specifically focusing on J- and H-type dimers (Figures S10 and S11 in the Supporting Information). These dimers play a critical role in determining the photophysical properties of the compounds, as they represent the primary interacting units within the aggregates. J-type dimers exhibit a characteristic slip angle that promotes constructive coupling between the transition dipole moments of the monomers, resulting in enhanced radiative decay and a red-shifted emission. In contrast, H-type dimers have a head-to-head configuration, leading to destructive dipole coupling and the formation of a "dark state," which suppresses radiative decay and is responsible for the observed blue-shifted absorption. These structural differences between J- and H-type dimers contribute significantly to the overall emission behavior and align well with the trends observed in our slip-angle analysis. From Figure S9, the organic molecules are initially away from each other, but as the simulation goes on, the molecules tend to be more closer leading to the formation of aggregates. The stronger intermolecular interactions in water lead to closer aggregation of molecules, whereas no significant molecular aggregation is observed in THF and methanol. Notably, the RDFs exhibit similar trends across all solvents, irrespective of the AIE activity of the molecules, indicating that RDF alone cannot distinguish between the AIE active and inactive molecules. Therefore, our findings suggest that, regardless of their AIE activity, molecules tend to aggregate in solvents like water and exhibit non-aggregative behavior in solvents such as THF and methanol.

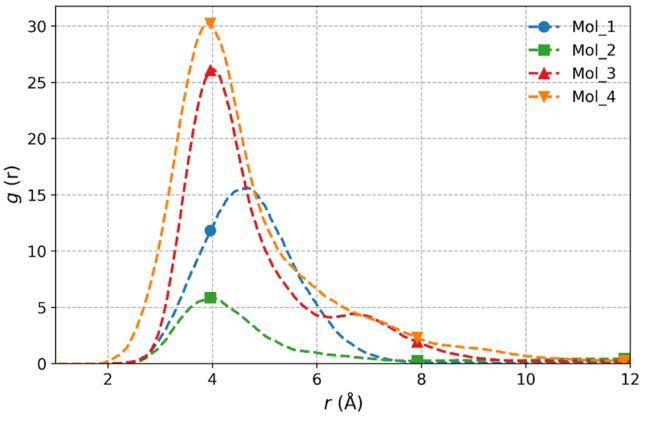


**Figure 4.** Center of mass radial distribution function (RDF) plots of the investigated compounds in a water environment obtained from MD simulated trajectories.

We evaluated the Gibbs free energy change of aggregation of two molecules, compound **1** (AIE-active) and compound **2** (AIE-inactive), surrounded by 2000 water molecules in GROMACS. We systematically varied the intermolecular distance during the simulation and assessed the corresponding free energy changes. These free energy profiles were obtained via Metadynamics simulations. Our results indicate that the free energy change associated with the transition from monomers to the aggregated state is negative for both molecules, regardless of their AIE activity. This negative free energy change suggests that aggregation is thermodynamically favorable. The free energy profiles are illustrated in Figure 7. As shown in Figure 7, for Compound **1**, the change in free energy is around −33 kJ/mol. For Compound **2**, the corresponding change is around −28 kJ/mol, as indicated by the blue and red lines, respectively (Figure 5).

**Slip Angle Analysis.** AIE is the phenomenon where a molecule, nonemissive or weakly emissive in its monomeric state, exhibits enhanced photoluminescence upon aggregation. This enhancement arises from restricting intramolecular motions in the aggregated state, reducing nonradiative decay pathways and favoring radiative decay. The type of aggregation, particularly the formation of J- or H-aggregates, plays a crucial role in determining the emission properties. Environmental factors also influence aggregation behavior and emission outcomes.

In solution, molecular aggregates typically form two common types: J-type and H-type. These aggregate structures arise due to interactions such as Coulombic and van der Waals forces between the molecules. These interactions can induce


https://doi.org/10.1021/acs.jpcb.4c03744
J. Phys. Chem. B XXXX, XXX, XXX−XXX

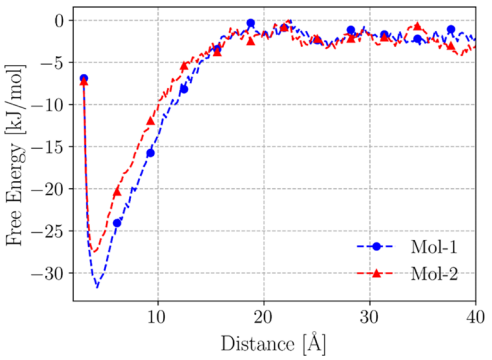


**Figure 5.** Behavior of the distance between the monomers versus the change in Gibbs free energies.

shifts in the energy levels of the molecules, either positively or negatively. J-type aggregates are characterized by a head-to-tail arrangement of molecules, leading to negative Coulombic interactions. This specific arrangement results in an optically allowed exciton state at a lower energy level. Consequently, the J-aggregate has a red-shifted absorption and emission spectrum compared to the monomer. This shift allows for enhanced emission as the exciton state in J-aggregates is energetically favorable for radiative decay. Additionally, the coherent coupling in J-aggregates facilitates delocalization of the exciton, reducing nonradiative losses and further contributing to the increased emission efficiency. In contrast, H-type aggregates form through a face-to-face stacking of molecules, leading to positive Coulombic interactions. This arrangement causes an upward shift in the exciton energy levels, resulting in an optically allowed exciton state at a higher energy level. Due to this shift, the emission from H-aggregates is typically quenched as the lowest-energy excited state ($S_1$) is nonemissive. This is because the excitation energy is trapped in higher-energy states that do not readily undergo radiative decay.

To characterize the aggregation patterns exhibited by the molecules, we conducted slip angle calculations, aiming to discern the types of aggregates formed. Previous studies have categorized aggregates into three main types: J-type, H-type, and X-type. Recent research[20] outlined that aggregates with slip angles less than 54.4° are classified as J-type, while those exceeding 54.4° are deemed H-type. In J-type aggregates, the transition from the first singlet excited state ($S_1$) to the ground state ($S_0$) is permitted, whereas it is forbidden in H-type aggregates. Consequently, molecules within H-type aggregates exhibit AIE inactivity, while those within J-type aggregates demonstrate AIE activity. Our slip angle calculations involved defining two vectors: $\Phi_1$, joining the center of mass between two molecules, and $\Phi_2$, extending from the molecule's center of mass to the nearest carbon atom within the same plane. The combined distribution of angles $\Phi_1$ and $\Phi_2$ is depicted in Figure 6. Notably, for AIE-active compound **1**, the distribution is denser toward values less than 54.4°, indicating a prevalence of J-type pairs. In contrast, in other cases, the distribution leans toward the right side, indicative of H-type pairs. This abundance of H-type pairs in inactive molecules impedes the $S_1$ to $S_0$ transition, rendering them AIE inactive.

Employing a cutoff distance of 3.5 nm from the molecule's center of mass, we further quantified the number of J and H pairs. Figure 7 illustrates the bar distribution of an exact number of J and H pairs, with blue predominating in the case of the active compound **1**. At the same time, red dominates for other compounds, reflecting the prevalence of H-type aggregates. Thus, the observed AIE inactivity in other compounds can be attributed to forming a more significant number of H-type pairs.

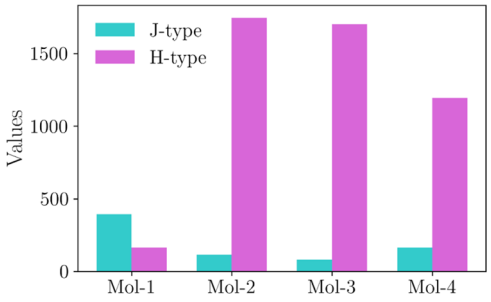


**Figure 7.** Number of J and H pairs in the morphology of organic molecules during the MD simulation. The cutoff criterion for calculating the pairs is 3.5 nm.

We have performed a detailed evaluation of representative dimers to provide a more rigorous classification of the J- and H-type dimers extracted from our MD simulations. In particular, we analyzed the oscillator strengths of the $S_1$ and $S_2$ excited states for both J- and H-type dimers. Our results demonstrate that J-type dimers exhibit a significantly higher oscillator strength for $S_1$ than $S_2$, which is consistent with the expected behavior of J-type aggregates where constructive dipole coupling enhances the transition dipole moment. On the other hand, H-type dimers show the opposite trend, with $S_1$ having a notably lower oscillator strength than $S_2$, indicating destructive dipole coupling and forming a dark state. The binding energies were calculated following the approach recommended in the ORCA 6.0 manual by Neese et al., which defines the binding energy as

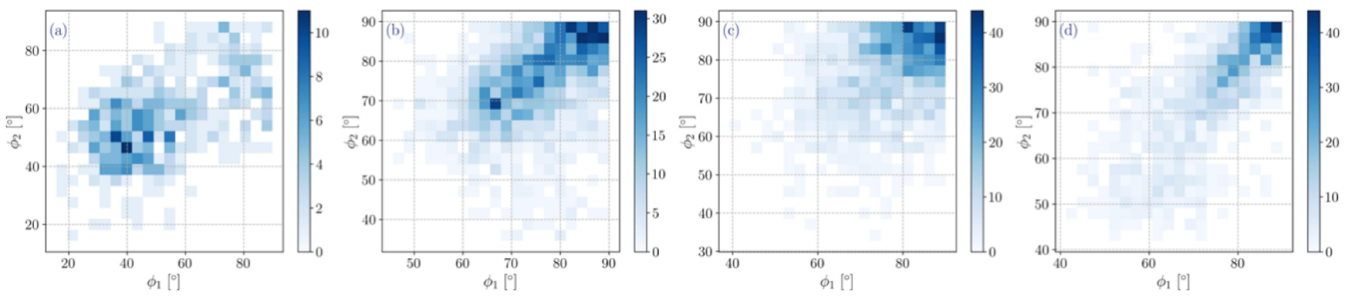


**Figure 6.** Combined distribution function plot of the investigated compounds [(a−d) corresponds to compounds **1**−**4** respectively].


https://doi.org/10.1021/acs.jpcb.4c03744
J. Phys. Chem. B XXXX, XXX, XXX−XXX

**Table 3. Symmetry Adapted Perturbation Theory (SAPT) Calculated Energy Components of the Investigated Compounds (kJ/mol) and the Number of J and H Pairs of the Molecules in the Aggregated State within a Distance of 3.5 nm**

| compounds | electrostatic | exchange | induction | dispersion | total | no. of j pairs | no. of h pairs |
|---|---|---|---|---|---|---|---|
| **1** | −11.3 | 21.3 | −4.9 | −41.3 | −36.1 | 393 | 163 |
| **2** | −9.2 | 10.0 | −2.6 | −15.1 | −16.9 | 114 | 1745 |
| **3** | −12.9 | 14.6 | −3.3 | −26.9 | −28.5 | 81 | 1703 |
| **4** | −10.1 | 14.1 | −3.3 | −18.7 | −17.9 | 164 | 1195 |

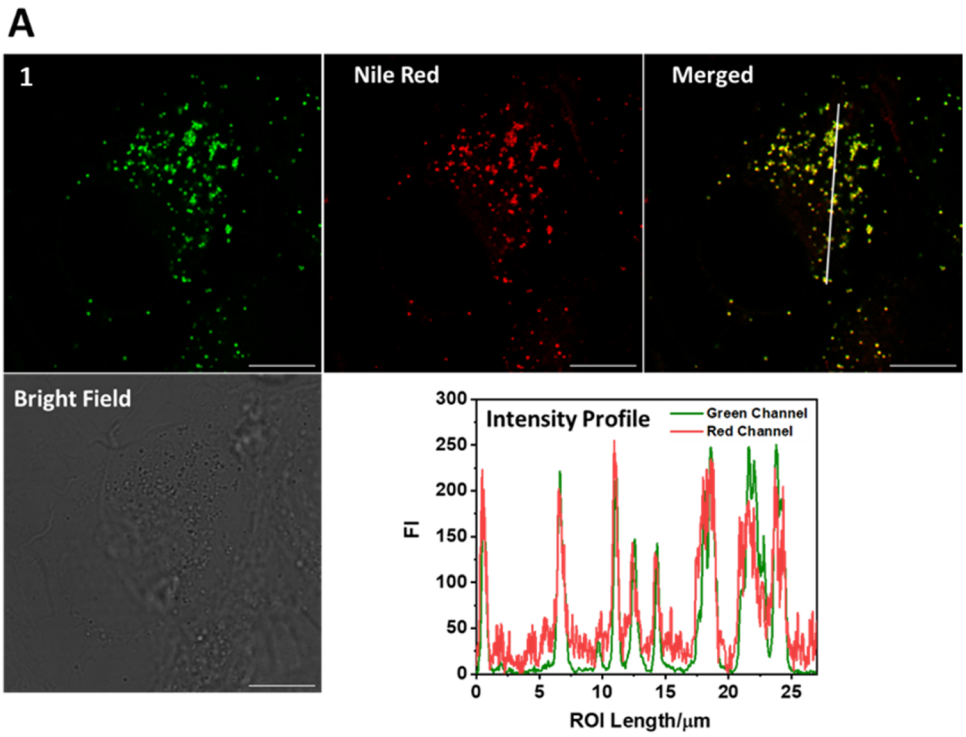


**Figure 8.** CLSM images of the compound (**1**), commercial marker (Nile-Red), merged, bright field, and intensity profile plots. Rr values for **1** are 0.89.

$$\text{B. E.} = E_{\text{dimer}}(\text{at near separation}) - E_{\text{dimer}}(\text{at larger separation})$$

This calculated binding energy accounts for intermolecular interactions in the context of both the ground and excited states, providing a more reliable comparison between them. The results in Table S3 show that, for all the investigated compounds, the binding energy in the excited state ($BE_{ex}$) is larger than in the ground state ($BE_{gs}$). This trend indicates stronger binding in the excited state, consistent with the excimer formation observed experimentally. Interestingly, for the AIE-active compound, the difference between $BE_{ex}$ and $BE_{gs}$ was found to be approximately 10 kJ/mol. This small difference, within the range of DFT accuracy, suggests that the binding strengths in the excited and ground states are similar, thus promoting emission. In contrast, for the AIE-inactive compounds, $BE_{ex}$ is significantly larger than $BE_{gs}$, which supports the notion of excimer formation leading to non-radiative decay. Our computational studies reveal that the molecule exhibiting enhanced emission in aqueous solution predominantly forms J-aggregates. This aggregation mode leads to a lower-energy exciton state conducive to efficient radiative decay, explaining the enhanced emission. On the other hand, the other synthesized molecules, which do not show enhanced emission, tend to form H-aggregates, resulting in quenching of their excited states and reduced emission. The formation of J-aggregates in the molecule with enhanced emission leads to a lower energy exciton state and efficient radiative decay, providing a logical and theoretical basis for the observed photophysical behavior. This phenomenon is further substantiated via QM calculations as tabulated in Table S4.

**SAPT Analysis.** In addition to our previous analyses, we employed symmetry-adapted perturbation theory calculations, with the DFT module and basis set 6-31+g(d,p), to support our findings further. The resulting values are compiled in Table 3, with calculations performed on dimer structures. Initially, dimers were configured in an H-type arrangement, and subsequent optimization was conducted using Gaussian 09 to obtain final structures for SAPT calculations. Examination of electrostatic and induction energies revealed consistency across all cases, while variations were observed in exchange (repulsive) and dispersion energies, influencing molecular alignment within the bulk. Specifically, compound **1** exhibited higher exchange energy values, indicative of stronger repulsive forces, leading to greater intermolecular distances than compounds **2**, **3**, or **4**. This observation is corroborated by RDF plots, where the first peak height is lower in compound **1**, reflecting a reduced probability of molecular proximity due to higher repulsive energies. Consequently, the quantitative analysis revealed fewer J or H pairs in compound **1** than other inactive compounds, attributed to increased repulsive


https://doi.org/10.1021/acs.jpcb.4c03744
J. Phys. Chem. B XXXX, XXX, XXX−XXX

energies between its monomers. Conversely, dispersion energies, responsible for maintaining molecular proximity, were also higher in compound **1**. These SAPT calculations provide valuable insights into the interplay of noncovalent interactions governing molecular aggregation, reinforcing our understanding of AIE behavior in the studied compounds.

**Live Cell Imaging.** The molecules are defined by the presence of donor and acceptor groups that yield intramolecular charge transfer behavior. Such molecules also have tremendous applications in the investigations of biomolecular environment.[41−43] The synthesized molecules are also characterized by 3,4,5-trimethoxyphenyl ring, an essential moiety for several biological pharmacophores, in particular, anticancer agents such as combretastatin-A4, colchicine, podophyllotoxin among others.[44,45] The molecules **1**−**4** are hydrophobic and have a biologically relevant scaffold. Therefore, they could be useful in investigating the membrane or lipid-rich organelles of the cell.[25,46,47] We first checked the effect of the compounds for their cellular toxicity, and the compounds showed no adverse impact (Figure S12). Upon incubating the fluorophores **1** and **2** with COS-7 cells, we observed punctate-like structures that could be associated with the lipid droplets. Lipid droplets are cellular organelles composed mainly of lipids, primarily triglycerides and cholesterol esters, surrounded by a phospholipid monolayer.[48] These droplets serve as storage sites for energy-rich lipids and play crucial roles in various physiological and pathological conditions, including obesity, metabolic disorders, and lipid-related diseases.[48] To indicate their localization, commercially available Nile Red, an established probe for the lipid droplets,[49] is incubated along with the molecules. The colocalization of molecules yielded an excellent overlap with Pearson's correlation coefficient (Rr) values of 0.89 for **1** (Figure 8) and 0.9 for **2** (Figure S12). The subcellular localization studies with molecules **3** and **4** also yielded strong correlation coefficients of 0.85 and 0.88, respectively (Figure S13). The localization propensity within the lipid droplets can be due to their inherent lipophilic nature. It naturally prefers a hydrophobic environment, such as lipid droplets, and can be utilized to provide insights into the function of the lipid droplets.

## CONCLUSIONS

In conclusion, we synthesized four organic molecules and investigated their photophysical properties and their potential for biological imaging. Utilizing a combination of experimental and computational techniques, including quantum mechanical and molecular dynamics calculations, we have advanced our understanding of their AIE characteristics. Our results indicate that the charge transfer nature and oscillator strength of the first singlet state alone cannot determine AIE activity. Instead, molecular dynamics simulations revealed that solvent interactions play a crucial role, with THF and methanol acting as good solvents, while water promotes aggregation of the synthesized molecules. Further analysis through slip angle calculations demonstrated that the orientation of molecules within aggregates significantly influences their AIE behavior. Specifically, AIE-active molecules tend to form J-type aggregates, whereas AIE-inactive molecules form H-type aggregates. These findings were corroborated by symmetry-adapted perturbation theory calculations, which provided additional theoretical support. This interdisciplinary study successfully bridges the gap between experimental observations and theoretical predictions, offering valuable insights into the complex interplay between molecular structure, aggregation behavior, and emission properties. Our work contributes to the fundamental understanding of AIE mechanisms and lays the groundwork for designing AIE-active materials with potential applications in advanced sensing and imaging technologies.

## ASSOCIATED CONTENT

### Supporting Information

The Supporting Information is available free of charge at https://pubs.acs.org/doi/10.1021/acs.jpcb.4c03744.

Supporting figures, tables and characterization spectral data are given (PDF)

## AUTHOR INFORMATION


### Corresponding Authors

**Sriram Kanvah** − *Department of Chemistry, Indian Institute of Technology Gandhinagar, Gandhinagar 382055, India;* orcid.org/0000-0002-6906-960X; Email: sriram@iitgn.ac.in

**Anirban Mondal** − *Department of Chemistry, Indian Institute of Technology Gandhinagar, Gandhinagar 382055, India;* orcid.org/0000-0003-3029-8840; Email: amondal@iitgn.ac.in

### Authors

**Deeksha Rajput** − *Department of Chemistry, Indian Institute of Technology Gandhinagar, Gandhinagar 382055, India*

**Sanyam** − *Department of Chemistry, Indian Institute of Technology Gandhinagar, Gandhinagar 382055, India;* orcid.org/0000-0001-7410-8207

**Gaurav Rawat** − *Department of Chemistry, Indian Institute of Technology Gandhinagar, Gandhinagar 382055, India*

**Priyanshu Sorout** − *Department of Chemistry, Indian Institute of Technology Gandhinagar, Gandhinagar 382055, India*

Complete contact information is available at: https://pubs.acs.org/10.1021/acs.jpcb.4c03744


### Author Contributions

†D.R. and Sanyam shares equal authorship. D.R. performed the overall investigation and methodology, including synthesis, photophysical studies, and cell biology experiments. G.R. assisted in the revisions. Sanyam and P.S. performed quantum mechanical calculations and molecular dynamics simulations. D.R. and Sanyam developed the first draft of the manuscript. S.K. supervised, planned, and conceived the experiment and was involved in manuscript editing, writing, and funding procurement. A.M. planned and supervised the simulations and was involved in manuscript writing and editing.

### Notes

The authors declare no competing financial interest.

## ACKNOWLEDGMENTS

S.K. acknowledges research funding from SERB (CRG/2022/007048). D.R. acknowledges a research fellowship from IIT Gandhinagar. Sanyam thanks CSIR for the fellowship. A.M., Sanyam, and P.S. thank PARAM Ananta for computational resources. Acknowledgements to Shabnam for general help during the revision stage.



https://doi.org/10.1021/acs.jpcb.4c03744
J. Phys. Chem. B XXXX, XXX, XXX−XXX

## REFERENCES


(1) Cai, Y.; Du, L.; Samedov, K.; Gu, X.; Qi, F.; Sung, H. H. Y.; Patrick, B. O.; Yan, Z.; Jiang, X.; Zhang, H.; et al. Deciphering the Working Mechanism of Aggregation-Induced Emission of Tetraphenylethylene Derivatives by Ultrafast Spectroscopy. *Chem. Sci.* **2018**, *9*, 4662−4670.

(2) Mei, J.; Leung, N. L.; Kwok, R. T.; Lam, J. W.; Tang, B. Z. J. C. r. Aggregation-Induced Emission: Together We Shine, United We Soar! *Chem. Rev.* **2015**, *115*, 11718−11940.

(3) An, B.-K.; Gierschner, J.; Park, S. Y. Π-Conjugated Cyanostilbene Derivatives: A Unique Self-Assembly Motif for Molecular Nanostructures with Enhanced Emission and Transport. *Acc. Chem. Res.* **2012**, *45*, 544−554.

(4) Cen, P.; Huang, J.; Jin, C.; Wang, J.; Wei, Y.; Zhang, H.; Tian, M. Aggregation-Induced Emission Luminogens for in Vivo Molecular Imaging and Theranostics in Cancer. *Aggregate* **2023**, *4*, No. e352.

(5) Guan, J.; Shen, C.; Peng, J.; Zheng, J. What Leads to Aggregation-Induced Emission? *J. Phys. Chem. Lett.* **2021**, *12*, 4218−4226.

(6) Hong, Y.; Lam, J. W. Y.; Tang, B. Z. Aggregation-Induced Emission: Phenomenon, Mechanism and Applications. *Chem. Commun.* **2009**, 4332−4353.

(7) Hernández, F. J.; Crespo-Otero, R. Modeling Excited States of Molecular Organic Aggregates for Optoelectronics. *Annu. Rev. Phys. Chem.* **2023**, *74*, 547−571.

(8) Feng, G.; Liu, B. Aggregation-Induced Emission (Aie) Dots: Emerging Theranostic Nanolights. *Acc. Chem. Res.* **2018**, *51*, 1404−1414.

(9) Dahiwadkar, R.; Rajput, D.; Singh, D.; Soppina, V.; Kanvah, S. Aie Active Cyanostilbenes for Live-Cell Imaging of Lipid Droplets. *New J. Chem.* **2023**, *47*, 10016−10024.

(10) Peng, Q.; Shuai, Z. Molecular Mechanism of Aggregation-Induced Emission. *Aggregate* **2021**, *2*, No. e91.

(11) Gierschner, J.; Lüer, L.; Milián-Medina, B.; Oelkrug, D.; Egelhaaf, H.-J. Highly Emissive H-Aggregates or Aggregation-Induced Emission Quenching? The Photophysics of All-Trans Para-Distyrylbenzene. *J. Phys. Chem. Lett.* **2013**, *4*, 2686−2697.

(12) Chau, J. H. C.; Lee, M. M. S.; Yu, E. Y.; Kwok, R. T. K.; Lam, J. W. Y.; Sun, J.; Tang, B. Z. Advances in Biomimetic Aie Nanoparticles for Diagnosis and Phototherapy. *Nanoscale* **2024**, *16*, 14707−14715.

(13) Jian, X.; Jiang, G.; Wang, J. Recent Advances of Aggregation-Induced Emission Luminogens for Point-of-Care Biosensing Systems. *Chem. Commun.* **2024**, *60*, 8484−8496.

(14) Mahalingavelar, P.; Kanvah, S. α-Cyanostilbene: A Multifunctional Spectral Engineering Motif. *Phys. Chem. Chem. Phys.* **2022**, *24*, 23049−23075.

(15) Kanvah, S.; Dahiwadkar, R.; Kaloo, M. A. Functional α-Cyanostilbenes: Sensing to Imaging. *Synlett* **2023**, *35*, 3−20.

(16) Gao, A.; Wang, Q.; Wu, H.; Zhao, J.-W.; Cao, X. Research Progress on Aie Cyanostilbene-Based Self-Assembly Gels: Design, Regulation and Applications. *Coord. Chem. Rev.* **2022**, *471*, 214753.

(17) Afrin, A.; Chinna Ayya Swamy, P. Symphony of Light: AIE and MFC in Carbazole-Based Cyanostilbenes. *J. Mater. Chem. C* **2024**, *12*, 1923−1944.

(18) Yamamoto, N. Mechanisms of Aggregation-Induced Emission and Photo/Thermal E/Z Isomerization of a Cyanostilbene Derivative: Theoretical Insights. *J. Phys. Chem. C* **2018**, *122*, 12434−12440.

(19) Yamamoto, N. Free Energy Profile Analysis to Identify Factors Activating the Aggregation-Induced Emission of a Cyanostilbene Derivative. *Phys. Chem. Chem. Phys.* **2021**, *23*, 1317−1324.

(20) Kreger, K.; Schmidt, H.-W.; Hildner, R. Tailoring the Excited-State Energy Landscape in Supramolecular Nanostructures. *Electronic Structure* **2021**, *3*, 023001.

(21) Kumari, B.; Paramasivam, M.; Mukherjee, T.; Khandelwal, S.; Dutta, A.; Kanvah, S. A Competitive Effect of Acceptor Substitutions on the Opto-Electronic Features of Triphenylamine Cored Di α-Cyanostilbene Derivatives. *New J. Chem.* **2021**, *45*, 4683−4693.

(22) Shen, X. Y.; Wang, Y. J.; Zhao, E.; Yuan, W. Z.; Liu, Y.; Lu, P.; Qin, A.; Ma, Y.; Sun, J. Z.; Tang, B. Z. Effects of Substitution with Donor−Acceptor Groups on the Properties of Tetraphenylethene Trimer: Aggregation-Induced Emission, Solvatochromism, and Mechanochromism. *J. Phys. Chem. C* **2013**, *117*, 7334−7347.

(23) Wang, L.; Qin, Y.; Cheng, Y.; Fan, W.; Yang, S.; Zheng, L.; Cao, Q. Intermolecular Hydrogen Bonds Induce Restriction of Access to the Dark State for Triggering Aggregation-Induced Emission. *J. Mater. Chem. C* **2022**, *10*, 5356−5363.

(24) Zhang, K.; Liu, J.; Zhang, Y.; Fan, J.; Wang, C.-K.; Lin, L. Theoretical Study of the Mechanism of Aggregation-Caused Quenching in near-Infrared Thermally Activated Delayed Fluorescence Molecules: Hydrogen-Bond Effect. *J. Phys. Chem. C* **2019**, *123*, 24705−24713.

(25) Zhang, F.; Wu, X.; Liu, B.; Han, T.; Yan, D.; Wang, D.; Zhong Tang, B. Emerging Designs of Aggregation-Induced Emission Luminogens for Lipid Droplets Imaging. *Coord. Chem. Rev.* **2023**, *493*, 215337.

(26) Chen, Y.; Jiang, H.; Hao, T.; Zhang, N.; Li, M.; Wang, X.; Wang, X.; Wei, W.; Zhao, J. Fluorogenic Reactions in Chemical Biology: Seeing Chemistry in Cells. *Chem. Biomed. Imaging* **2023**, *1*, 590−619.

(27) Chen, H.; Liu, L.; Qian, K.; et al. Bioinspired Large Stokes Shift Small Molecular Dyes for Biomedical Fluorescence Imaging. *Sci. Adv.* **2022**, *8*, No. eabo3289.

(28) Wang, H.; Li, Q.; Alam, P.; et al. Aggregation-Induced Emission (AIE), Life and Health. *ACS Nano* **2023**, *17*, 14347−14405.

(29) Frisch, M.; Trucks, G. W.; Schlegel, H. B.; Scuseria, G. E.; Robb, M. A.; Cheeseman, J. R.; Scalmani, G.; Barone, V.; Mennucci, B.; Petersson, G. A. *Gaussian 09*; Gaussian. Inc: Wallingford CT, 2009, Vol. 121, pp 150−166.

(30) Kerru, N.; Gummidi, L.; Bhaskaruni, S. V. H. S.; Maddila, S. N.; Singh, P.; Jonnalagadda, S. B. A Comparison between Observed and DFT Calculations on Structure of 5-(4-Chlorophenyl)-2-Amino-1,3,4-Thiadiazole. *Sci. Rep.* **2019**, *9*, No. 19280.

(31) Barone, V.; Cossi, M. Quantum Calculation of Molecular Energies and Energy Gradients in Solution by a Conductor Solvent Model. *J. Phys. Chem. A* **1998**, *102*, 1995−2001.

(32) Neese, F. The Orca Program System. *WIREs Computational Molecular Science* **2012**, *2*, 73−78.

(33) Jorgensen, W. L.; Tirado-Rives, J. Potential Energy Functions for Atomic-Level Simulations of Water and Organic and Biomolecular Systems. *Proc. Natl. Acad. Sci. U.S.A.* **2005**, *102*, 6665−6670.

(34) Jorgensen, W. L.; Tirado-Rives, J. The Opls [Optimized Potentials for Liquid Simulations] Potential Functions for Proteins, Energy Minimizations for Crystals of Cyclic Peptides and Crambin. *J. Am. Chem. Soc.* **1988**, *110*, 1657−1666.

(35) Hess, B.; Kutzner, C.; van der Spoel, D.; Lindahl, E. Gromacs 4: Algorithms for Highly Efficient, Load-Balanced, and Scalable Molecular Simulation. *J. Chem. Theory Comput.* **2008**, *4*, 435−447.

(36) Pronk, S.; Páll, S.; Schulz, R.; et al. Gromacs 4.5: A High-Throughput and Highly Parallel Open Source Molecular Simulation Toolkit. *Bioinformatics* **2013**, *29*, 845−854.

(37) Berendsen, H. J. C.; Postma, J. P. M.; van Gunsteren, W. F.; DiNola, A.; Haak, J. R. Molecular Dynamics with Coupling to an External Bath. *J. Chem. Phys.* **1984**, *81*, 3684−3690.

(38) Smith, D. G. A.; Burns, L. A.; Simmonett, A. C.; et al. Psi4 1.4: Open-Source Software for High-Throughput Quantum Chemistry. *J. Chem. Phys.* **2020**, *152*, 184108.

(39) Kumari, B.; Yadav, A.; Pany, S. P.; Pradeepkumar, P. I.; Kanvah, S. Cationic Red Emitting Fluorophore: A Light up Nir Fluorescent Probe for G4-DNA. *J. Photochem. Photobiol. B, Biol.* **2019**, *190*, 128−136.

(40) Fu, H.; Cui, M.; Zhao, L.; Tu, P.; Zhou, K.; Dai, J.; Liu, B. Highly Sensitive near-Infrared Fluorophores for in Vivo Detection of Amyloid-B Plaques in Alzheimer's Disease. *J. Med. Chem.* **2015**, *58*, 6972−6983.

(41) Pivovarenko, V. G.; Klymchenko, A. S. Fluorescent Probes Based on Charge and Proton Transfer for Probing Biomolecular Environment. *Chem. Rec.* **2024**, *24*, No. e202300321.




https://doi.org/10.1021/acs.jpcb.4c03744
J. Phys. Chem. B XXXX, XXX, XXX−XXX

(42) Abeywickrama, C. S. Large Stokes Shift Benzothiazolium Cyanine Dyes with Improved Intramolecular Charge Transfer (Ict) for Cell Imaging Applications. *Chem. Commun.* **2022**, *58*, 9855−9869.
(43) Yan, C.; Zhu, Z.; Yao, Y.; Wang, Q.; Guo, Z.; Zhu, W.-H. Engineering near-Infrared Fluorescent Probes Based on Modulation of Molecular Excited States. *Acc. Mater. Res.* **2024**, *5*, 64−75.
(44) Negi, A. S.; Gautam, Y.; Alam, S.; Chanda, D.; Luqman, S.; Sarkar, J.; Khan, F.; Konwar, R. Natural Antitubulin Agents: Importance of 3,4,5-Trimethoxyphenyl Fragment. *Bioorg. Med. Chem.* **2015**, *23*, 373−389.
(45) Langarizadeh, M. A.; Ameri, A.; Tavakoli, M. R.; Abiri, A.; Forootanfar, H. The Trimethoxyphenyl (Tmp) Functional Group: A Versatile Pharmacophore. *Med. Chem. Res.* **2023**, *32*, 2473−2500.
(46) Thiam, A. R.; Farese, R. V., Jr; Walther, T. C. The Biophysics and Cell Biology of Lipid Droplets. *Nat. Rev. Mol. Cell Biol.* **2013**, *14*, 775−786.
(47) Brasaemle, D. L.; Wolins, N. E. Packaging of Fat: An Evolving Model of Lipid Droplet Assembly and Expansion. *J. Biol. Chem.* **2012**, *287*, 2273−2279.
(48) Olzmann, J. A.; Carvalho, P. Dynamics and Functions of Lipid Droplets. *Nat. Rev. Mol. Cell Biol.* **2019**, *20*, 137−155.
(49) Greenspan, P.; Mayer, E. P.; Fowler, S. D. Nile Red: A Selective Fluorescent Stain for Intracellular Lipid Droplets. *J. Cell Biol.* **1985**, *100*, 965−973.


https://doi.org/10.1021/acs.jpcb.4c03744
*J. Phys. Chem. B* XXXX, XXX, XXX−XXX